Time-resolved laser-induced incandescence characterization of metal nanoparticles

T. A. Sipkens[1] · N. R. Singh[1] · K. J. Daun[1]

Abstract This paper presents a comparative analysis of time-resolved laser-induced incandescence measurements of iron, silver, and molybdenum aerosols. Both the variation of peak temperature with fluence and the temperature decay curves strongly depend on the melting point and latent heat of vaporization of the nanoparticles. Recovered nanoparticle sizes are consistent with ex situ analysis, while thermal accommodation coefficients follow expected trends with gas molecular mass and structure. Nevertheless, there remain several unanswered questions and unexplained behaviors: the radiative properties of laser-energized iron nanoparticles do not match those of bulk molten iron; the absorption cross sections of molten iron and silver at the excitation laser wavelength exceed theoretical predictions; and there is an unexplained feature in the temperature decay of laser-energized molybdenum nanoparticles immediately following the laser pulse.

1 Introduction

Metal nanoparticles have a myriad of existing and emerging applications due to their unique size-dependent chemical and electromagnetic properties, which differ significantly from those of bulk materials [1]. For instance, they have been used for optical devices [2], antimicrobial coatings [3], heterogeneous catalysis [4], and environmental remediation [5]. Gas-phase reactors offer an economical route toward large-scale production, although it is also imperative to obtain a carefully controlled size distribution, since nanoparticle functionality depends strongly on size. This can be an especially challenging constraint, since the local conditions within these reactors are often poorly characterized and the fundamental transport and chemical processes underlying nanoparticle formation and growth are not completely understood [6]. Accordingly, there is a need for laser-based diagnostics that can provide spatially- and temporally-resolved information about the nanoparticle sizes to develop a fundamental understanding of the nanoparticle synthesis process and, eventually, to permit online control of the nanoparticle fabrication process. While the literature often focuses on the benefits of metal nanoparticles, there is also a growing understanding about their unintended and adverse effects on human health [7] and the environment [8]. For example, metal nanoparticles produced by industrial plasma cutting and welding are known to cause bronchitis, pneumonia, and metal fume fever [9]. As such, there is also a need to size aerosolized metal nanoparticles from an occupational hygiene perspective.

Time-resolved laser-induced incandescence (TiRe-LII), mainly used as a diagnostic for sizing soot primary particles in combustion applications [10], appears to be a promising tool to fulfill these needs. In this procedure a pulsed laser rapidly heats a sample volume of nanoparticles, and their spectral incandescence is measured as the nanoparticles thermally equilibrate with the surrounding gas. The spectral incandescence data are used to derive an instantaneous effective temperature using a spectroscopic model that accounts for the nanoparticle spectral emission cross section. Since the observed temperature decay is a function of nanoparticle size, in principle it is possible to infer the nanoparticle size distribution by regressing simulated temperatures, obtained with a heat transfer model, to the

✉ T. A. Sipkens
  tsipkens@uwaterloo.ca

1 Department of Mechanical and Mechatronics Engineering, University of Waterloo, 200 University Ave. W., Waterloo, ON N2L 3G1, Canada

pyrometrically-inferred values. The heat transfer model incorporates properties that include the density, specific heat capacity, and latent heat of vaporization of the bulk materials, as well as the thermal accommodation coefficient (TAC or α), which defines the average energy transfer as a gas molecule scatters from the energized nanoparticle.

Vander Wal et al.'s pioneering measurements on iron, tungsten, titanium, and molybdenum nanoparticles [11] focused on establishing the feasibility of TiRe-LII size characterization by making spectrally and temporally resolved emission measurements using a gated spectrometer and photomultiplier tubes, respectively. These measurements indicated that the observed spectral emission appeared to be mainly due to incandescence, albeit with some non-incandescent laser-induced emission occurring at both the laser pulse and 200 ns after the laser pulse, of undetermined origin. Subsequent LII studies of metal nanoparticles have probed aerosolized iron [12–18], molybdenum [19–21], nickel [22], silver [23, 24], tungsten [25], and silicon [26] nanoparticles. (Solid silicon is a semiconductor, but metalizes upon melting [27].) A subset of these measurements have attempted to infer the nanoparticle diameter, d_p, or size distribution, $p(d_p)$, but the reliability of these measurements is limited by uncertainty in the heat transfer models needed to interpret the LII data, chiefly focused around the thermal accommodation coefficient [22] and how it may vary with bath gas composition. In the case of materials having a moderate melting point, such as iron and silicon nanoparticles, estimates of the nanoparticle size and TAC can be obtained simultaneously because both evaporation and conduction heat transfer modes influence the detectable temperature decay [14, 16, 26]. This is not generally possible for refractory materials such as molybdenum [20, 21] and tungsten or low-melting-point materials like silver [24]. Alternatively, the TAC may be calculated through molecular dynamics simulations [28]; preliminary work shows good agreement between simulated and experimentally-derived TACs [16], but the reliability of this approach has yet to be fully established.

The accuracy and reliability of LII-inferred parameters is also impaired by uncertainties in the spectroscopic model that relates the measured laser-induced emission to the nanoparticle temperature. Since nanoparticles are usually much smaller than the absorption and emission wavelengths, their spectral absorption cross section is proportional to $E(\mathbf{m}_\lambda) = -\mathrm{Im}[(\mathbf{m}_\lambda - 1)^2/(\mathbf{m}_\lambda + 2)^2]$, where $\mathbf{m}_\lambda = n - ik$ is the complex refractive index. Many LII studies on metal nanoparticles simply assume that $E(\mathbf{m}_\lambda)$ is uniform over the measurement wavelengths (e.g., [12–15, 21]), which the authors justify due to a perceived lack of available information about the optical properties of the hot metal nanoparticles. On the contrary, however, the optical properties of most metals at high temperature have been characterized experimentally [29] and, particularly for molten metals, have a theoretical basis in Drude theory [30].

This paper presents a comparative assessment of two-color TiRe-LII measurements on iron, silver, and molybdenum nanoparticles in a variety of bath gases. These materials were selected to highlight the varying information contained in the TiRe-LII data for metal nanoparticles in different states and cooling models dominated by different heat transfer modes. Following Ref. [16], and in contrast to other LII studies which exclusively consider nanoparticles synthesized in the gas phase, in this work the nanoparticles are dispersed in a colloid and then aerosolized using a pneumatic atomizer. This approach enables investigation of a range of aerosols that could not be synthesized in the gas phase. Moreover, in contrast to gas-phase synthesis, in which the bath gas composition and local conditions strongly influence on the nanoparticle size distribution, in this experiment the sizes of each type of nanoparticle are expected to be identical for all bath gas, which further facilitates a comparative analysis.

The remainder of the paper is organized as follows: The spectroscopic and heat transfer models used to interpret the TiRe-LII data are presented, followed by a discussion of the experimental apparatus and procedure, including the steps followed for synthesis and ex situ characterization of the nanocolloid. Next, the peak temperatures obtained for a range of laser fluences are presented for the three types of nanoparticles considered in this study; differences in these curves are attributed to the differing melting points and latent heats of vaporization for the bulk material. The peak effective temperatures are also used to infer a minimum absorption cross section at the laser wavelength through calorimetry. A comparative analysis of temperature decay curves also highlights the differing amounts of information contained in the TiRe-LII data, depending on the heat transfer modes important to nanoparticle cooling. Recovered nanoparticle sizes and thermal accommodation coefficients match expected values and trends based on theory and other experiments in the literature, but the results also show some unanswered questions that can only be resolved through further experimental and theoretical analysis.

2 LII measurement model

2.1 Spectroscopic model

TiRe-LII signals are due to the emission from all nanoparticle size classes in the aerosol measurement volume. At any instant, the spectral incandescence of the laser-energized nanoparticles is

$$J_\lambda(t) = C_\lambda \int_0^\infty p(d_\mathrm{p}) \frac{\pi d_\mathrm{p}^2}{4} Q_{\mathrm{abs},\lambda}(d_\mathrm{p}, \lambda) I_{\mathrm{b},\lambda}[T_\mathrm{p}(t, d_\mathrm{p})] d(d_\mathrm{p})$$

(1)

where C_λ is a constant that accounts for the nanoparticle volume fraction, collection optics geometry, and photoelectric efficiency of the detectors, d_p is the nanoparticle diameter, $p(d_\mathrm{p})$ is the nanoparticle size distribution, $Q_{\mathrm{abs},\lambda}(d_\mathrm{p})$ is the absorption efficiency, T_p is the nanoparticle temperature, and $I_{\mathrm{b},\lambda}[(T_\mathrm{p}(t,d_\mathrm{p})]$ is the blackbody intensity. The $Q_{\mathrm{abs},\lambda}(d_\mathrm{p}) \cdot \pi d_\mathrm{p}^2/4$ factor is a function of nanoparticle diameter and wavelength that acts to modify the blackbody intensity. Since the nanoparticles are expected to have diameters smaller than the detection wavelengths and the laser excitation wavelength, their spectral absorption cross section can be modelled using the Rayleigh limit of Mie theory [31]

$$Q_{\mathrm{abs},\lambda} = -4x \, \mathrm{Im}\left(\frac{\mathbf{m}_\lambda^2 - 1}{\mathbf{m}_\lambda^2 + 2}\right) = 4x E(\mathbf{m}_\lambda)$$

(2)

where $\mathbf{m}_\lambda = n_\lambda + ik_\lambda$ is the complex index of refraction, $E(\mathbf{m}_\lambda)$ is the absorption function, and $x = \pi d_\mathrm{p}/\lambda$ is the size parameter. Alternatively, Eq. (2) can be written in terms of complex electrical permittivity, $\boldsymbol{\varepsilon}_\lambda = \varepsilon_{\mathrm{I},\lambda} + i\varepsilon_{\mathrm{II},\lambda}$

$$Q_{\mathrm{abs},\lambda} = -4x \, \mathrm{Im}\left[\frac{\boldsymbol{\varepsilon}_\lambda - 1}{\boldsymbol{\varepsilon}_\lambda + 2}\right] = 4x E(\boldsymbol{\varepsilon}_\lambda)$$

(3)

In two-color (or autocorrelated) LII, the spectral incandescence measured at two wavelengths is used to derive an effective pyrometric temperature

$$\begin{aligned} T_\mathrm{p}^{\mathrm{eff}}(t) &= \frac{hc_0}{k_\mathrm{B}}\left(\frac{1}{\lambda_2} - \frac{1}{\lambda_1}\right)\left[\ln\left(\frac{J_{\lambda_1}(t)}{J_{\lambda_2}(t)} \frac{E(\mathbf{m}_{\lambda_2})}{E(\mathbf{m}_{\lambda_1})}\left(\frac{\lambda_1}{\lambda_2}\right)^6\right)\right]^{-1} \\ &= \frac{hc_0}{k_\mathrm{B}}\left(\frac{1}{\lambda_2} - \frac{1}{\lambda_1}\right)\left[\ln\left(\frac{J_{\lambda_\mathrm{r}}(t)\lambda_\mathrm{r}^6}{E(\mathbf{m})_\mathrm{r}}\right)\right]^{-1} \end{aligned}$$

(4)

where h is Planck's constant, c_0 is the speed of light in a vacuum, k_B is the Boltzmann constant, λ_1 and λ_2 are the detection wavelengths, and $E(\mathbf{m}_{\lambda 1})/E(\mathbf{m}_{\lambda 2})$ is the ratio of the emission efficiencies at the detector wavelengths. Henceforth the spectral incandescence, wavelengths, and $E(\mathbf{m}_\lambda)$ ratios are abbreviated as $J_{\lambda\mathrm{r}}$, λ_r, and $E(\mathbf{m})_\mathrm{r}$, respectively. If d_p is monodisperse, $T_\mathrm{p}^{\mathrm{eff}}$ corresponds to the true nanoparticle temperature, provided that J_λ is due to incandescence, and not some other type of laser-induced emission. For polydisperse aerosols, $T_\mathrm{p}^{\mathrm{eff}}$ will be an average temperature, biased toward the larger nanoparticles due to their larger emission cross sections and, at longer cooling times, their higher temperatures.

In the case of soot, $E(\mathbf{m}_\lambda)$ is particularly challenging to quantify due to its complex composition and morphology, which can vary considerably with fuel chemistry and local conditions [32, 33]. Consequently, uncertainty in $E(\mathbf{m}_\lambda)$ remains one of the main factors that limits the reliability of LII-derived properties of soot [34]. In principle, the spectral absorption cross sections of metallic nanoparticles are known with much greater certainty; they have a well-defined, homogenous composition, and the dielectric properties of the bulk material apply directly to nanoparticles provided the nanoparticle diameter is much larger than the mean free electron path [1, 29]. Moreover, the bulk dielectric properties of most metals at high temperatures have been derived from ellipsometry measurements made under carefully controlled conditions, and, in the case of liquid metal nanoparticles, have an underpinning in Drude theory [31], in which the electromagnetic wave is coupled to the internal energy of the metal by nearly free electrons that collide with more massive ions as the electrons accelerate and decelerate in the fluctuating electronic field. According to this theory,

$$\varepsilon_1(\omega) = n^2 - k^2 = 1 - \frac{\omega_\mathrm{p}^2 \tau^2}{1 + \omega^2 \tau^2}$$

(5)

and

$$\varepsilon_2(\omega) = 2nk = \frac{\omega_\mathrm{p}^2 \tau}{\omega(1 + \omega^2 \tau^2)}$$

(6)

where $\omega = 2\pi c_0/\lambda$ is the angular frequency of the electromagnetic field, τ is the relaxation time (average time between electron collisions), and ω_p is the plasma frequency. The plasma frequency is given by

$$\omega_\mathrm{p}^2 = \frac{N^{*2}e^2}{m_e \varepsilon_0}$$

(7)

where N^* is the effective number of free electrons per unit volume, m_e and e are the rest mass and charge of an electron, respectively, and ε_0 is the vacuum permittivity. The free electron density can be found from the atomic density, assuming that the number of electrons contributed to the conduction band by each atom is equal to the valence, adjusted by a factor that accounts for band structure. In principle, the relaxation time is related to the DC conductivity in the limit of $\omega \to 0$,

$$\sigma_{\mathrm{DC}} = \frac{N^* e^2 \tau}{m_e}$$

(8)

The optical properties of molten silver are well represented by Drude theory, since the 4 eV energy gap between the highest core electron state (4d) and conduction band [35] corresponds to ultraviolet wavelengths. Consequently,

Fig. 1 (*left*) Real and imaginary components of the refractive index and (*right*) $E(\mathbf{m}_\lambda)$ values for molten iron (*top*), molten silver (*middle*) and solid molybdenum (*bottom*). *Solid curves* denote values used to analyze the LII data
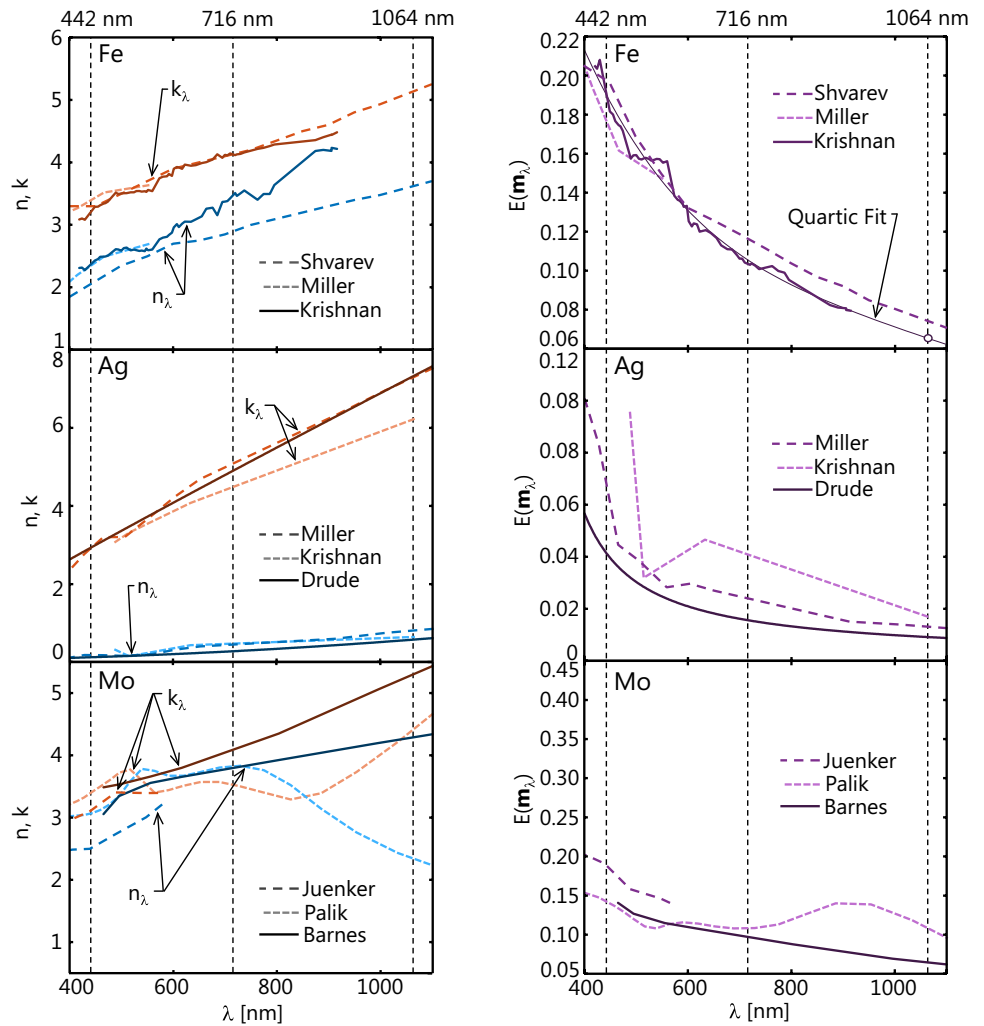
photon absorption and emission within the wavelengths important to LII are entirely due to electronic transitions within the conduction band. Indeed, Fig. 1 shows excellent agreement between the refractive indices determined from ellipsoidal measurements on molten silver [35] and parameters found from Eqs. (5) and (6), using an effective electron number density of $N^*/N = 1.05$ [35, 36] (which corresponds to $\omega_p = 1.3175 \times 10^{15}$ rad/s and $\tau = 3.7823 \times 10^{-15}$ s).

The situation for molten iron nanoparticles is more complicated. As a transition metal, the d-band electrons overlap the conduction band, so the radiative properties in the visible and infrared spectrum are due to both interband and intraband transitions. Consequently, while the general trends in $\boldsymbol{\varepsilon}_\lambda$ (or $\mathbf{m}_\lambda$) are consistent with Drude theory, Eqs. (5) through (8) are not expected to provide an accurate representation of $E(\mathbf{m}_\lambda)$. Previous TiRe-LII measurements by Sipkens et al. [16] on molten iron nanoparticles used a Drude model from Kobatake et al. [37] that was later shown to be non-physical [38]. In this work, we initially consider

experimental data derived from ellipsometry measurements from Krishnan et al. [39] and Shvarev et al. [40] shown in Fig. 1, which are consistent with those of Miller [35].

While the laser-energized iron and silver nanoparticles are in the molten state during LII detection, the molybdenum nanoparticles presumably remain solid given the high melting temperature of molybdenum (2896 K [41]). The n_λ, k_λ, and $E(\mathbf{m}_\lambda)$ values for solid molybdenum depend on temperature through DC conductivity via Drude/Hagen–Rubens theory [42], although these theories cannot be applied directly due mainly to the strong impact electronic band structure in the solid state. Instead, n_λ, k_λ are taken from reflectance measurements on solid molybdenum at 2200 K between 465 and 2000 nm [43]. Figure 1 shows the comparison of these data to similar data reported by Juenker et al. [44] at 2200 K and wavelengths shorter than 576 nm and data compiled by Palik [45] at room temperature.

Values of n_λ, k_λ, and $E(\mathbf{m}_\lambda)$ at the detection and excitation wavelengths are summarized in Table 1. A comparison

Table 1 Bulk radiative properties used to interpret TiRe-LII measurements on Fe, Ag, and Mo nanoparticles

	442 nm			716 nm			$E(\mathbf{m})_r$	1064 nm		
	n_λ	k_λ	$E(\mathbf{m}_\lambda)$	n_λ	k_λ	$E(\mathbf{m}_\lambda)$		n_λ	k_λ	$E(\mathbf{m}_\lambda)$
Ag (Drude)	0.10	2.92	0.041	0.25	4.89	0.015	2.67	0.55	7.31	0.009
Fe [39]	2.37	3.21	0.191	3.48	4.13	0.103	1.85	5.64[a]	5.01[a]	0.065[a]
Fe [40]	2.06	3.30	0.198	2.90	4.13	0.116	1.70	3.62	5.13	0.073
Mo [43]	2.83	3.45	0.152	3.83	4.09	0.097	1.59	4.29	5.30	0.065

[a] Values are obtained by extrapolation

Table 2 Physical properties of iron, silver, and molybdenum

Property	Fe	Ag	Mo
ρ (kg/m^3)	$8171 - 0.64985 \cdot T_p$ [46]	$9346 - 0.9067 \cdot (T_p - 1234)$ [47]	$9100 - 0.6 \cdot (T_p - T_m), T_p \geq T_m$ $9100 - 0.5 \cdot (T_p - T_m), T_p < T_m$ [41]
c_p [J/(kg K)]	835 [48]	531 [49]	$56.5 + 0.01177 \cdot (T_p - T_m), T_p \geq T_m$ $a(T_p)^a, T_p < T_m$ [41]
T_m (K)	1811 [48]	1234 [47]	2896 [41]
K (J/kg), Eq. (16)	7.11×10^6	2.83×10^6	7.29×10^6
T_b (K)	3134 [50]	2466 [51]	4913 [52]
$\Delta H_{v,b}$ (J/kg)	6.09×10^6 [50]	2.35×10^6 [51]	6.23×10^6 [53]
T_{cr} (K)	9340 [54]	6410 [47]	14,588 [54]
A (Pa), Eq. (14)	4.70×10^{10}	2.43×10^{10}	2.31×10^{11}
γ_s (N/m)	$1.865 - (T_p - 1823) \cdot (0.35) \cdot (10^{-3})$ [55]	$1.0994 - 0.0002 \cdot T_p$ [56]	2.11 [57]

[a] $a(T_p) = (1582 + 0.0589 \cdot (T_p - T_m)) \cdot (3.0 + 1.03 \cdot (10^{-3}) \cdot (T_p - T_m))$

of the results reveals that the n_λ and k_λ trends for molten iron and silver are similar ($n_\lambda < k_\lambda$, both increase monotonically with wavelength), which is expected from Drude free electron theory (though the d-band electron contributions in molten iron preclude a quantitative Drude model [38]). In contrast, n_λ and k_λ are similar in magnitude for solid molybdenum, possibly due to strong interband contributions. In terms of the spectral absorption cross section, $E(\mathbf{m}_\lambda)$ for silver is much smaller than iron and molybdenum nanoparticles due to its higher electrical conductivity. The physicality of these presumed values will be revisited later in the paper.

2.2 Heat transfer model

Modelling the incandescence during nanoparticle cooling requires $T_p(d_p, t)$, which is found by simultaneously solving

$$c_p m_p \frac{dT_p}{dt} = -q_{evap}(T_p, d_p) - q_{cond}(T_p, d_p) - q_{rad}(T_p, d_p) \tag{9}$$

and

$$\frac{dm_p}{dt} = -\dot{m}_{evap}(T, d_p) \tag{10}$$

where c_p is the specific heat capacity of the aerosolized nanoparticle, m_p is the mass of the nanoparticle, q_{evap}, q_{cond},

and q_{rad} are the heat transfer rates due to evaporation, conduction, and thermal radiation, respectively, and $\dot{m}_{evap}$ is the mass loss due to evaporation. The nanoparticle diameter changes over time as a result of mass loss and thermal expansion and is given by

$$d_p(T, m_p) = \left[\frac{6m_p}{\pi \rho(T)} \right]^{1/3} \tag{11}$$

where $\rho(T)$ is the density of the nanoparticle as a function of the temperature. The initial nanoparticle diameter, $d_{p,o}$, is related to the initial mass and the density

$$d_{p,o} = \left[\frac{6m_{p,o}}{\pi \rho_o} \right]^{1/3} \tag{12}$$

where ρ_o is the nominal density of the nanoparticle at equilibrium in the aerosol and $m_{p,o}$ is the initial nanoparticle mass, which acts as the initial condition for Eq. (10). The density, specific heat capacity, and other bulk thermophysical properties used in the heat transfer model are summarized in Table 2 for silver, iron, and molybdenum.

The nanoparticle sizes are expected to be equal to or smaller than the mean free path within the carrier gases, so evaporation and conduction heat transfer occur within the free molecular regime, which assumes that gas and vapor
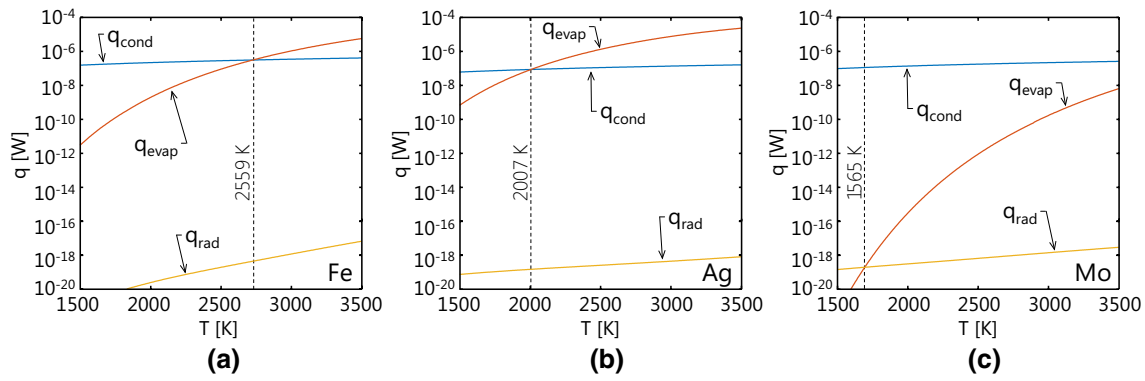
Fig. 2 Heat transfer from **a** iron, **b** silver, and **c** molybdenum nanoparticles in argon at 300 K and 101.3 kPa, assuming $d_p = 50$ nm and $\alpha = 0.1$. *Vertical dashed lines* show the temperatures at which the dominant heat transfer mode changes. The relative importance of the heat transfer modes over the observed temperature decays determines the quantities that can be inferred from the TiRe-LII data

molecules travel between the nanoparticle and equilibrium gas without undergoing intermolecular collisions in the vicinity of the nanoparticle. Free molecular evaporation is given by

$$q_{evap}(T_p, d_p) = \Delta H_v \pi d_p^2 N_v'' \beta = \Delta H_v \pi d_p^2 \frac{n_v c_v}{4} \beta \qquad (13)$$

where ΔH_v is the heat of vaporization of the metal atoms (J/atom), N_v'' is the vapor number flux (atoms/m²), $n_v = P_v/(k_B T_g)$ is the vapor number density, c_v is the mean thermal speed of the vapor, β is the sticking coefficient, which is assumed to be unity, and P_v is the vapor pressure. Assuming that the molten nanoparticle surface and its vapor above the surface are in quasi-equilibrium, the Clausius–Clapeyron equation can be used to relate the heat of vaporization and the vapor pressure,

$$P_{v,o} = A \exp\left(\frac{-\Delta H_v}{R_s} \frac{1}{T_p}\right) \qquad (14)$$

where R_s is the specific gas constant, A is a material constant in Pa, and $P_{v,o}$ is the vapor pressure in Pa. Since this pressure value corresponds to a flat interface between the two phases, this value can be further modified to account for the increased surface energy due to nanoparticle curvature using the Kelvin equation [16]

$$P_v = P_{v,o} \exp\left[\frac{4\gamma_s(T_p)}{d_p \rho(T_p) R_s T_p}\right] \qquad (15)$$

where $\gamma_s(T_p)$ is the surface tension of the nanoparticle. The heat of vaporization is given by Watson's equation [26, 58]

$$\Delta H_v(T_p) = K\left(1 - \frac{T_p}{T_{cr}}\right)^{0.38} \qquad (16)$$

where K is a material constant and T_{cr} is the critical temperature. Values of A, K, T_b, $\Delta H_{v,b}$, and T_{cr} for iron, silver, and molybdenum are listed in Table 2.

Free molecular heat conduction is given by

$$q_{cond}(T_p, d_p) = \pi d_p^2 N_g'' \langle E_o - E_i \rangle = \pi d_p^2 \frac{n_g c_{g,t}}{4} \langle E_o - E_i \rangle \qquad (17)$$

where N_g'' is the incident gas number flux, $n_g = P_g/(k_B T_g)$ is the molecular number density of the carrier gas, $c_{g,t} = [8k_B T_g/(\pi m_g)]^{1/2}$ is the mean thermal speed of the carrier gas, P_g, T_g, and m_g are the carrier gas pressure, temperature, and molecular mass, respectively, and $\langle E_o - E_i \rangle$ is the average energy transfer per collision. The latter term can be rewritten using the TAC, α,

$$\langle E_o - E_i \rangle = \alpha \langle E_o - E_i \rangle_{max} = \alpha\left(2 + \zeta_{rot}/2\right) k_B\left(T_p - T_g\right) \qquad (18)$$

where ζ_{rot} is the number of rotational degrees of freedom of the carrier gas. Monatomic gases have no rotational modes available, so $\zeta_{rot} = 0$, while the linear polyatomic gases, such as N_2 and CO_2, have $\zeta_{rot} = 2$. Substituting Eq. (18) in Eq. (17) results in

$$q_{cond}(T_p, d_p) = \alpha \pi d_p^2 \frac{P_g c_{g,t}}{4T_g}\left(2 + \frac{\zeta_{rot}}{2}\right)\left(T_p - T_g\right) \qquad (19)$$

Finally, thermal radiation heat transfer from the nanoparticle is given by

$$q_{rad}(T_p, d_p) = 4\pi \int_0^\infty Q_{abs,\lambda}(d_p) \frac{\pi d_p^2}{4} I_{b,\lambda}(T_p) d\lambda \qquad (20)$$

where $Q_{abs,\lambda}$ comes from Eq. (2) or Eq. (3). This calculation assumes that absorbed incident radiation is negligible, which

Fig. 3 Schematic of the experimental apparatus used in this study. A motive gas and nanoparticle colloid streams are combined in a pneumatic aerosolizer. Water from the colloid is removed from the sample using a diffusion dryer. The nanoparticles are then characterized with an TiRe-LII measurement in a sample chamber used with an Artium 200 M system
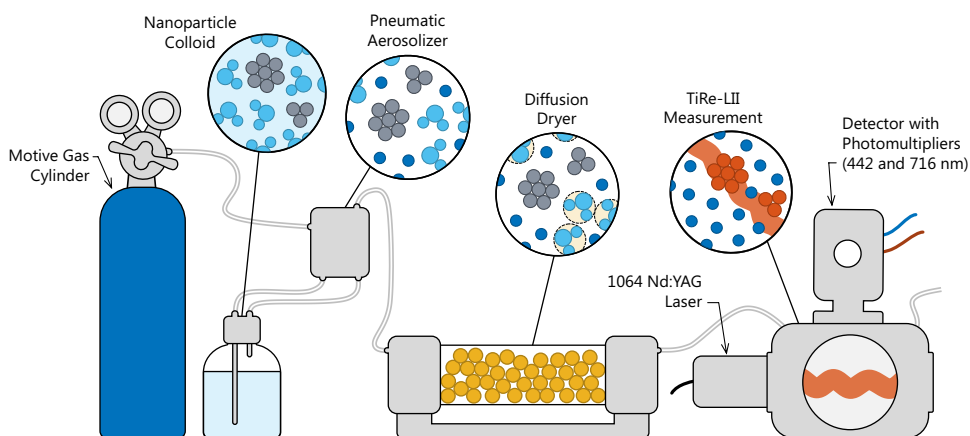
is reasonable since the surroundings are at a much lower temperature compared to the laser-energized nanoparticle.

Figure 2 shows simulated heat transfer modes plotted over the expected temperature range during the cooling stage for laser-energized silver, iron, and molybdenum nanoparticles in argon, assuming $\alpha = 0.1$, $d_p = 50$ nm, $T_g = 300$ K, and $P_g = 101.3$ kPa. In the case of molten iron and silver, evaporation heat transfer dominates at temperatures beyond approximately 2728 K and 2007 K, respectively. It is significant that, in the case of silver, evaporation heat transfer dominates over the range of LII-detectable temperatures, while, for iron nanoparticles, some of the observed cooling curve is dominated by conduction. Heat transfer from molybdenum is due almost entirely to conduction over the entire range of measurement temperatures. These observations impact the parameters that can be inferred from the TiRe-LII data, as discussed later in the paper. While thermal incandescence is the detection mechanism that underlies LII, in all three cases radiation heat transfer is orders of magnitude less than the other two heat transfer modes over the detection temperatures, so it is excluded from the remainder of the analysis.

3 Experimental apparatus and nanoparticle preparation

A schematic of the experimental apparatus is shown in Fig. 3. Motive gas flows through a TSI Model 3076 pneumatic atomizer operating in recirculation mode connected to a sample vessel containing a colloid suspension of either iron, silver, or molybdenum nanoparticles. Motive gases are supplied to the atomizer at a pressure of 200 kPa; under these conditions the atomizer is expected to produce an aerosol of droplets having a median diameter of 0.3 μm with a geometric standard deviation of less than 2.0 [59]. The colloid is diluted so that, on average, each droplet contains one nanoparticle. The droplets pass through a diffusion

drier charged with a silica gel desiccant, which removes any residual water and water-based contaminants from the nanoparticle synthesis from the aerosol stream. The dried aerosol then enters the sample chamber within which the TiRe-LII measurement is carried out. The pressure within the sample chamber was monitored using a pressure transducer and was observed to be within ± 5 kPa of atmospheric pressure throughout all experiments.

The TiRe-LII measurement is carried out with an Artium 200 M system, which uses a pulsed Nd:YAG laser operating at 1064 nm and 10 Hz to rapidly heat the nanoparticles within the probe volume defined by the intersection of the laser beam and solid angle of the detection optics. Relay imaging is used to obtain a 2.5 mm × 2.5 mm beam profile at the probe volume having a nearly top-hat temporally averaged fluence profile. The nominal laser fluence used in this study is 0.29 ± 0.03 J/cm^2 (found by measuring the pulse energy with a Coherent J-25MB-IR pyroelectric sensor and dividing by the beam area) and is adjusted by varying the Q-switch delay. The spectral incandescence is imaged onto two photomultipliers equipped with narrow bandpass filters centered at 442 and 716 nm (full width at half maximum of 50 nm). PMT voltages are sampled every 2 ns using a fast oscilloscope.

Iron and silver nanoparticle colloids were prepared in situ shortly before the TiRe-LII experiment to avoid agglomeration or oxidation of the nanoparticles. The molybdenum colloid was formed by dispersing a commercially available molybdenum nanopowder in deionized water. Zero-valent iron nanoparticles were synthesized by reducing ferrous iron ions (Fe^{2+}) in a solution of sodium borohydride ($NaBH_4$), used as the reducing agent, and carboxymethylcellulose (CMC), to prevent agglomeration in deionized water (DI-H_2O), following Refs. [60, 61]. To prepare the iron colloid, 8.29 g of iron (II) sulfate heptahydrate ($FeSO_4 \cdot 7H_2O$) was dissolved in 25 mL DI-H_2O and then added to 60 mL of CMC solution (14 g/L, ca. 250 kDa) under vigorous mixing for approximately 10 min

Fig. 4 Sample SEM image of silver nanoparticles (*left*) and TEM image of molybdenum nanoparticles (*right*) used in the current experiments. The silver nanoparticles appear as isolated spheres. In the case of molybdenum nanoparticles, the DLS measurements suggest that agglomeration occurs on the TEM grid
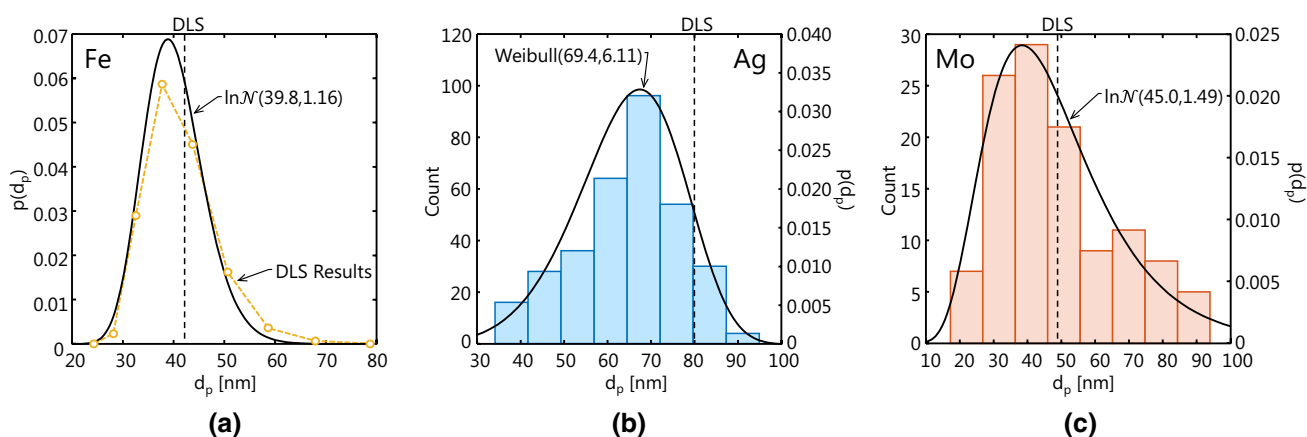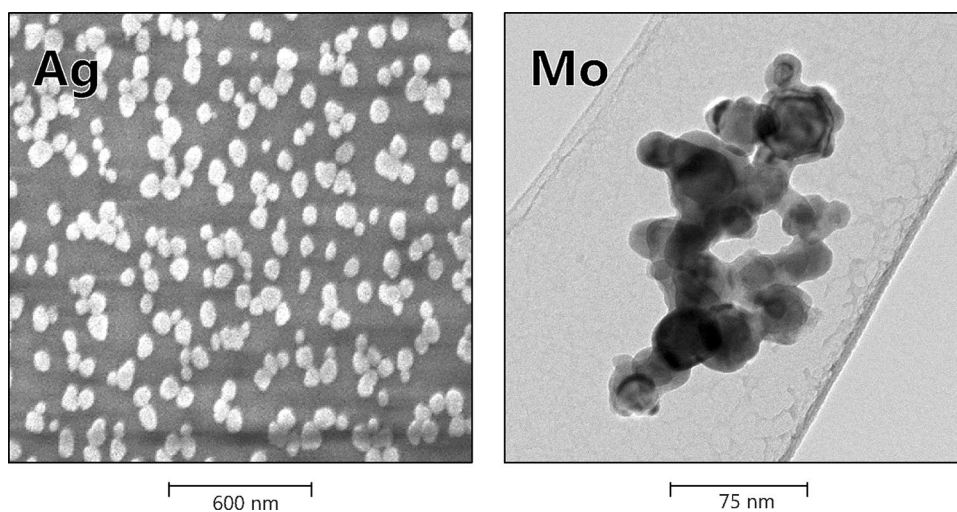

Fig. 5 Histogram showing an analysis of ex situ measured nanoparticle sizes for **a** iron (DLS), **b** silver (SEM), and **c** molybdenum (TEM). Histograms bins are obtained from electron microscopy image analysis

to ensure the formation of the CMC-Fe^{2+} complex. Separately, 1.13 g of NaBH$_4$ was dissolved in 15 mL of DI-H$_2$O and then slowly added to the CMC-Fe^{2+} solution, resulting in a black colloid, signifying the reduction of CMC-Fe^{2+} to CMC-Fe^0.

Silver nanoparticles were synthesized in solution using the procedure described in Ref. [62]. A reflux condenser was attached to a three-necked round-bottom flask, filled with 100 mL of deionized water, and kept under a nitrogen gas atmosphere. Using a glass pipette, 1.7 mL of a 1% silver nitrate aqueous solution was added to the round-bottom flask and the mixture was brought to a boil using a heating mantle for 15 min. Next, 2 mL of 1% citrate solution was then added to the reaction solution with a glass pipette. The solution was left to reflux under vigorous mechanical stirring for 1 h. The heating mantle was turned off, and the solution was allowed to cool to room temperature before being stored in an amber glass bottle until usage.

Molybdenum nanopowder (<100 nm) was purchased from Sigma-Aldrich (batch number MKBR4618V) and used without further purification. A 0.5 g sample of nanopowder was dispersed in 100 mL of DI-H$_2$O for 10 min using an ultrasonicator.

Additional ex situ characterization of the nanocolloid was performed to compliment or inform the TiRe-LII inference. Transmission and scanning electron microscopy (TEM, SEM) were used to image the molybdenum and silver nanoparticles, respectively, by placing a diluted aliquot of the colloid on a 200-mesh copper grid. Figure 4 shows sample electron microscopy images, and nanoparticle size histograms obtained from image analysis are shown in Fig. 5. Molybdenum nanoparticle sizes obey a lognormal distribution having a geometric mean (median) of 49 nm and a geometric standard deviation, σ_g, of 1.49, consistent with a self-preserving particle size distribution [63]. (The TEM images show aggregates of nanospheres,

Fig. 6 A sample of **a** single-shot incandescence signals (normalized to the peak) and **b** average effective temperature decay for TiRe-LII measurements on iron nanoparticles in argon
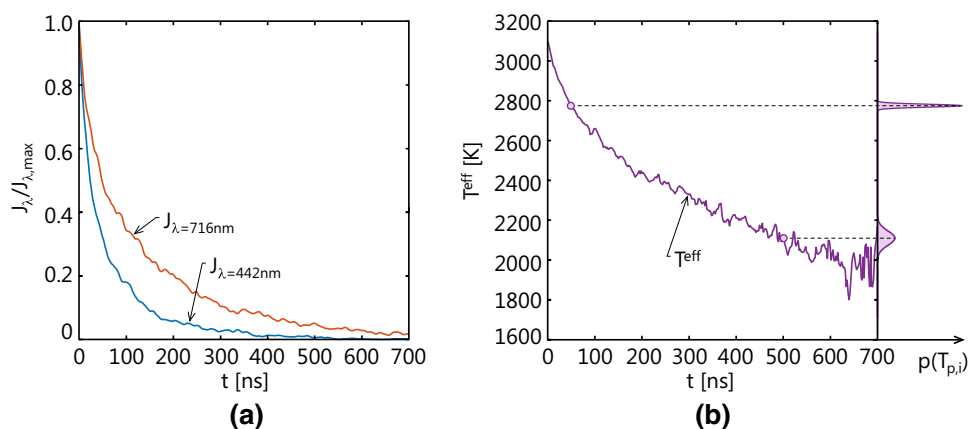
and agglomeration likely occurred on the TEM grid as the solvent evaporated and not within the nanocolloid.) Silver nanoparticle sizes obey a narrower, Weibull-type size distribution [64], with a mean diameter of 65 nm. For the remainder of the analysis silver nanoparticle diameters are treated as monodisperse. No useable SEM or TEM images of iron nanoparticles were obtained due to the extreme amount of oxidation that occurred between sample extraction and microscopy.

Dynamic light scattering (DLS) analysis was also performed on samples of each nanocolloid, which were diluted by a 1:1000 ratio in DI-H_2O and then ultrasonicated for approximately 10 min immediately before measurement. The measurement was carried out using a Vasco DL 135 instrument using a Padé–Laplace model to fit the data. The solid index of refractions was used for silver [65] and molybdenum [66], and a value of 2.87 was used for the CMC-coated iron nanoparticles [67]. All three samples showed a nanoparticle size that quickly increased during the DLS measurements, which is attributed to settling and agglomeration of the colloid. Mean nanoparticle diameters observed near the time of ultrasonication were found to be 42, 80, and 51 nm for iron, silver, and molybdenum, respectively. (In the case of molybdenum, the DLS measurement supports the hypothesis that agglomeration occurs on the TEM grid, and the nanoparticle size within the nanocolloid and aerosol corresponds to the primary particle diameter.) An approximation of the distribution for iron nanoparticles is also given in Fig. 5. Like the silver nanoparticles, the iron nanoparticle sizes obey a narrow distribution which is approximated as monodisperse throughout the rest of this work.

4 TiRe-LII analysis

Spectral incandescence traces from 250, 500, and 500 individual shots for iron, silver, and molybdenum, are

subdivided into groups of three and then averaged to reduce measurement variance. A set of pyrometric temperatures at each cooling time is then found using Eq. (4), and outliers are removed using a Thompson Tau procedure [68]. The resulting mean values are normally distributed, by the central limit theorem, and the parameters of these distributions (the expected mean and standard deviation of the mean) are used in subsequent analysis. Figure 6a shows sample single-shot experimental traces at each of the considered wavelengths (442 and 716 nm), normalized to the peak. Figure 6b shows an example temperature decay of the nanoparticles, following the above procedure. The distributions on the vertical axis correspond to the distribution of the mean at two instances in the cooling curve; at later times, the decreased signal-to-noise ratio causes these distributions to widen greatly.

4.1 Fluence study

We first investigate how changing the laser fluence affects the pyrometrically defined peak temperature. The laser energy was controlled by varying the laser flashlamp Q-switch delay between 137 and 250 μs, which corresponds to laser energies ranging from 18 to 4 mJ, respectively. The resulting fluence curves are shown in Fig. 7. Error bars are excluded for clarity and generally correspond to less than 10% of the recorded value.

To better understand the trends of $T_{p,max}$ with fluence, an interpolating function is derived considering the expected asymptotic behavior of the fluence curve, following Churchill and Usagi [69]. At low fluences/temperatures, the peak temperature should increase approximately linearly with increasing fluence, as the absorbed laser energy is directly proportional to the increase in sensible energy of the nanoparticles. At high fluences/temperatures, the curve should "plateau" since additional heat inputs to the nanoparticle increase the evaporation rate instead of the sensible energy of the nanoparticle. This behavior has been
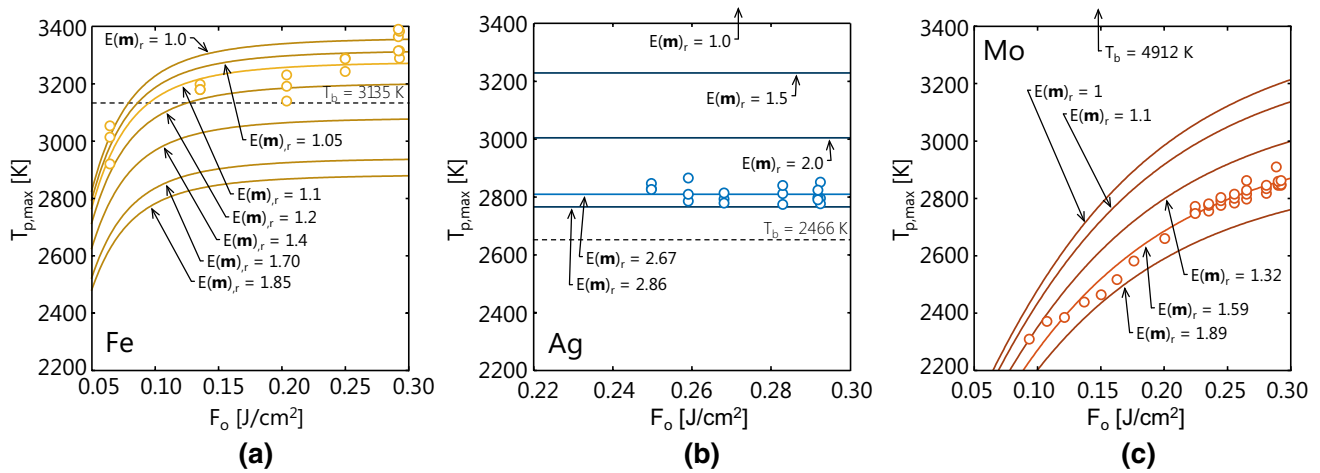
Fig. 7 Examination of the peak temperature, $T_{p,max}$, as a function of laser fluence for **a** iron, **b** silver, and **c** molybdenum

observed in other LII experiments on carbonaceous nanoparticles [70–72] and molybdenum nanoparticles by Eremin and Gurentsov [21]. Consequently, we assume a form

$$T_{p,max} = \left[(AF_0 + B)^n + C^n \right]^{1/n} \qquad (21)$$

where A, B, and C are fitting parameters and n is taken to be -3. One would expect that B would approximate the gas temperature (i.e., the nanoparticle temperature when $F_0 = 0$). The plateau temperature, C, should be slightly higher than the boiling point due to the fact that laser energy is added to the nanoparticle faster than it can be removed through evaporation, which is limited by the Clausius–Clapeyron equation. Consequently, the excess laser energy "accumulated" during the pulse causes a superheat, typically on the order of several hundred degrees Kelvin.

The trend of $T_{p,max}$ versus fluence for iron nanoparticles shows the progression from the linear toward the plateau region described above. While the general shape of $T_{p,max}$ verses F_0 for iron nanoparticles complies with the expected trend, the temperature of the plateau region calculated using $E_{m,r} = 1.85$ is approximately 2800 K, below the boiling point of bulk iron, 3135 K [50]. (The reduction in boiling point predicted by the Kelvin equation is only ~10 K for the ex situ-determined nanoparticle sizes.) More reasonable peak temperatures can be obtained using $E(\mathbf{m})_r = 1.1$, which is smaller than that expected using experimentally derived radiative properties of molten iron [35, 39] but consistent with previous TiRe-LII studies that matched TiRe-LII-inferred nanoparticle sizes to TEM-derived values by assuming $E(\mathbf{m})_r = 1$ [12, 14]. This treatment will be revisited later in the manuscript.

The peak temperatures of silver nanoparticles remain nearly constant with increasing laser fluence, suggesting that the silver nanoparticles are superheated and the additional laser heating roughly balances with an increased evaporation rate. Interpreting the spectral incandescence data with $E(\mathbf{m})_r = 2.67$ obtained from Drude theory results in a maximum peak temperature ~200 K above the boiling temperature, in line with the expected superheat, while using a value of $E(\mathbf{m})_r = 1$ results in a temperature of ~3600 K, which is likely non-physical.

The peak temperatures of the molybdenum nanoparticles increase approximately linearly with increasing F_0 for fluences up to 0.2 J/cm². Some degree of curvature in the fluence curve at higher fluences may suggest some sublimation, but using $E(\mathbf{m})_r = 1.59$ derived from ellipsometry measurements on polished molybdenum [43] gives peak temperatures below the melting point of molybdenum, 2896 K [41], suggesting that these nanoparticles remain solid. While the increased surface energy of nanoparticles can reduce their melting point relative to that of the bulk material by an amount proportional to $1/d_p$ [73, 74], given the relatively large size of the molybdenum nanoparticles anticipated from ex situ analysis, it seems unlikely that this effect would play a significant role in the present study.

The radiative properties of the nanoparticles can be further investigated by performing an energy balance during the heat-up phase of the TiRe-LII measurement, following Eremin et al. [13] and Sipkens et al. [16],

$$\rho(T_g) \frac{\pi d_p^3}{6} \left[H°(T_{p,max}) - H°(T_g) \right] = q_{laser} - q_{cond} - q_{evap} \qquad (22)$$

where $H°(T_g)$ and $H°(T_{p,max})$ are the enthalpy of the material at T_g and $T_{p,max}$, and

$$q_{laser} = \frac{\pi d_p^2}{4} Q_{abs,\lambda_{laser}} F_0 \qquad (23)$$
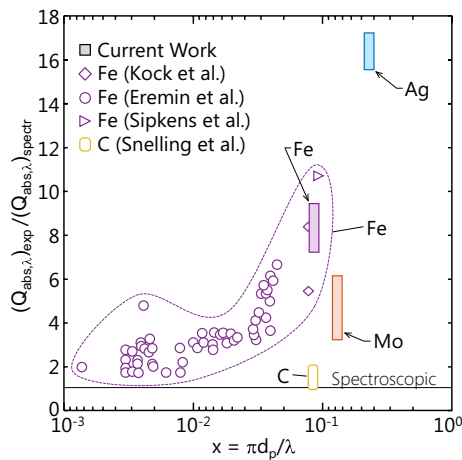
Fig. 8 Trends in the ratio of the LII-derived to spectroscopic absorption cross section at the laser wavelength (1064 nm) with increasing dimensionless size parameter, x. Data are taken from fluence studies by Eremin et al. (iron) [13], Kock et al. (iron) [14], Sipkens et al. (iron) [16], Snelling et al. (carbon) [75] and the current work (iron, silver, and molybdenum)

is the total energy absorbed by the nanoparticle, where F_0 is the laser fluence. Substituting Eq. (23) in Eq. (22), and neglecting evaporation and conduction losses during laser heating, gives the minimum $Q_{abs,\lambda}$ needed for the nanoparticles to reach the observed peak temperature.

Figure 8 shows trends in the ratio between the spectral absorption cross sections inferred from LII experiments to that from spectroscopic measurements versus size parameter, $x = \pi d_p / \lambda$. The height of the bar symbols corresponds to the spread across the various fluences considered in the present study. In the case of iron, silver, and molybdenum the spectroscopic absorption cross sections are taken from data reported in Refs. [39], [35], and [43], respectively. Snelling et al. [75] considered a series of ex situ measurements on soot. The height of the bar symbols indicates this variability. The results show that the calorimetrically derived absorption cross section at 1064 nm far exceeds the spectroscopic values for iron and silver nanoparticles, while the ones for molybdenum and carbon are closer to predicted values. One difference between these two cases is that there would be more evaporated material during laser excitation of iron and silver nanoparticles compared to molybdenum and soot. It may be possible that the combination of evaporated atoms and free electrons forms a plasma surrounding the nanoparticle that couples with the laser pulse and heats the nanoparticle through inverse Bremsstrahlung heating. Following this hypothesis, the apparent dependence of absorption cross section on nanoparticle size could be related to the work function/ionization potential of metal nanoparticles, which is inversely proportional to diameter [76]. Further theoretical

and experimental investigation is required to confirm this hypothesis, however.

4.2 Nanoparticle sizing and thermal accommodation coefficient

We next attempt to infer the nanoparticle size and thermal accommodation coefficient from a subset of the observed temperature decay curves. For this portion of the study the nominal fluence of 0.29 J/cm^2 is used for all TiRe-LII measurements. The analysis is carried out using temperatures starting from 30 ns after the peak temperature (unless otherwise noted), to avoid residual laser heating and known uncertainties associated with pyrometry during the laser pulse [26], and extending to a time at which a specified signal-to-noise ratio is exceeded. Estimates must be considered in the context of: (1) experimental uncertainty caused by photonic shot noise, electronic noise, and fluctuations in laser intensity; and (2) parameter uncertainties in the spectroscopic and heat transfer model parameters. We consider these two sources of uncertainty separately.

Measurement noise is characterized by examining the pyrometric temperatures using the $E(\mathbf{m})_r$ values described in Sect. 2.1 for silver and molybdenum nanoparticles, and $E(\mathbf{m})_r = 1.1$ for the iron nanoparticles, per Sect. 4.1; this treatment will be re-evaluated below. As noted above, the central limit theorem confirms that the mean pyrometric temperature, $T_{p,i}$, at the ith measurement time obeys a normal distribution with a mean and variance. Furthermore, inspection of the covariance matrix for the vector of temperatures at different cooling times reveals negligible covariance (off-diagonal) terms as one would expect from measurement noise dominated by photonic shot noise, which affects each temperature measurement independently. Consequently, the probability of the pyrometric temperature at each instant is given as

$$p\left(T_{p,i}\right) = p(b_i) = \mathcal{N}\left(\mu_i, \sigma_{\mu,i}^2\right) \qquad (24)$$

where μ_i is the mean, $\sigma_{\mu,i}^2 = \sigma_i^2 / n_i$ is the variance of the mean, and n_i is the number of samples. The joint probability density of the quantities of interest, $\mathbf{x} = [d_p, \alpha]^T$, conditional on the observed data $\mathbf{b} = [T_{p,1}, T_{p,2}, \ldots, T_{p,m}]^T$ is given by the joint normal distribution

$$p(\mathbf{x}|\mathbf{b}) = p(\mathbf{b}|\mathbf{x}) = \frac{1}{(2\pi)^{m/2} \prod\limits_{i=1}^{m} \sigma_{\mu,i}}$$

$$\exp\left\{ -\sum_{i=1}^{m} \frac{\left[\mu_i - T_{p,i}(\mathbf{x}, t_i)\right]^2}{2\sigma_{\mu,i}^2} \right\} \qquad (25)$$

where $p(\mathbf{b}|\mathbf{x})$ is the likelihood of the observed data occurring for a hypothetical set of model parameters. The
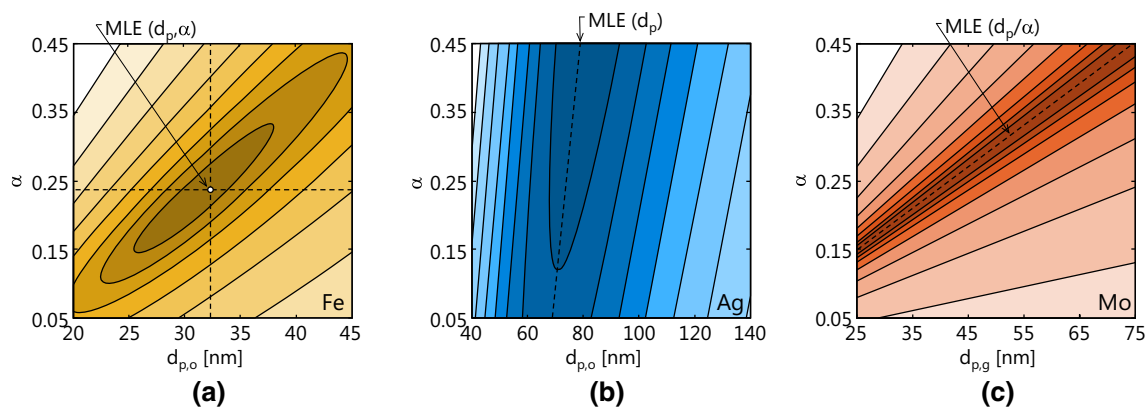
Fig. 9 Log contours of the likelihood function for **a** Fe–Ar, **b** Ag–Ar, and **c** Mo–Ar. The length of the domain of α is a consistent across all three plots. In the case of Mo–Ar, $\sigma_g = 1.49$

Table 3 Distribution width of multiplicative factors on model input parameters, θ_i

θ_i	$2\sigma_{\theta_i}/\mu_{\theta_i}$		
	Fe	Ag	Mo
$d_{p,g}$	–	–	0.10
σ_g	–	–	0.10
α	–	0.38	0.10[a]
T_g	0.01	0.01	0.01
ρ	0.10	0.10	0.10
C_p	0.10	0.10	0.10
ΔH_v	0.10	0.10	–
$\ln(A)$	0.01	0.01	–
T_i	0.004	0.004	0.004
$E_{m,r}$	0.10	0.10	0.20

Values correspond to two relative standard deviations, $2\sigma_{\theta_i}/\mu_{\theta_i}$

[a] This value is only used when inferring $d_{p,g}$ and σ_g. In this case, α is inferred and therefore not perturbed as part of θ

modelled temperatures are calculated using the nominal properties shown in Table 2. Marginalized probabilities for d_p and α are found by "integrating out" the influence of the other variable [77], which are nearly Gaussian. These probability densities are summarized by 95% credibility intervals, which, for a normal distribution, corresponds to $\pm 2\sigma_x$.

Contours of the log-likelihood function plotted in Fig. 9 for iron, silver, and molybdenum nanoparticles in argon reveal a robust maximum likelihood estimate, $\mathbf{x}_{MLE} = \arg\max[p(\mathbf{b}|\mathbf{x})]$ for the iron nanoparticles, but not for silver and molybdenum nanoparticles. The different likelihood topographies arise from the fact that different cooling regimes are observable for each type of nanoparticle, cf. Fig. 2. In the case of iron nanoparticles, the observed temperature decay is due to both evaporation heat transfer, which depends on d_p, and conduction heat transfer, which

depends on d_p and α. In contrast, the observed temperature decay for silver nanoparticles is almost entirely due to evaporative cooling, which depends on d_p but not α. Finally, the likelihood function for molybdenum nanoparticles is maximized not by a single point, but rather by a locus of solutions corresponding to a fixed value of α/d_p. One would expect this, since the observed temperature decay is entirely due to free molecular conduction, and under these circumstances rearrangement of Eq. (9) results in $dT_p/dt \simeq C \cdot \alpha/d_p \cdot [T_p(t) - T_g]$, so independent estimates of α and d_p cannot be inferred from a conduction-dominated temperature decay [20].

Parameter uncertainty is estimated using a Monte Carlo procedure, following a procedure similar to Crosland et al. [78]. In this approach we specify normal probability densities for the model parameters centered on the nominal values in Table 2 and with two relative standard deviations shown in Table 3. These distribution widths are chosen based on expected parameter uncertainties (e.g., variations in literature values and reported experimental uncertainty). Randomly sampled model parameters are substituted in the heat transfer model, and $\mathbf{x}_{MLE}$ is solved by nonlinear least-squares regression of modelled data and the pyrometric temperatures, i.e., minimizing the summation in Eq. (25). The recovered parameters obey near-Gaussian probability densities with widths that define the uncertainties in d_p and α, induced by model parameter uncertainty. The distribution widths due to measurement noise and model parameter uncertainty are reported separately, but they can be combined to provide an overall uncertainty estimate.

Table 4 summarizes the nanoparticle size and thermal accommodation coefficients found from TiRe-LII measurements on iron nanoparticles in argon, nitrogen, and carbon dioxide, for values of $E(\mathbf{m})_r$ equal to 1.1, 1.70, and 1.84. (The latter two values are from ellipsometry data in Refs. [40] and [39], respectively.) The recovered

Table 4 Maximum likelihood estimates of parameters of interest, x_i, for iron nanoparticles in different gases

Gas	x_i	$E_{m,r} = 1.1$				$E_{m,r} = 1.70$	$E_{m,r} = 1.84$	α, Molecular dynamics
		MLE	Experimental $\pm$	Parameter $\pm$	Corr.	MLE	MLE	
Ar	$d_{p,o}$	32.3	0.5	9.2	0.91	11.4	9.6	0.11
	α	0.24	<0.01	0.06		0.08	0.07	
N_2	$d_{p,o}$	30.2	0.4	8.3	0.91	10.7	9.0	–
	α	0.07	<0.01	0.02		0.02	0.02	
CO_2	$d_{p,o}$	28.2	0.6	8.2	0.91	10.1	8.5	–
	α	0.12	<0.01	0.03		0.04	0.03	

Estimates of uncertainty are broken into those resulting from noise in the measured signal and those resulting from sensitivity to input parameters, θ_i. Uncertainties correspond to 95% confidence level (two standard deviations). Nanoparticle sizes are given in nanometers
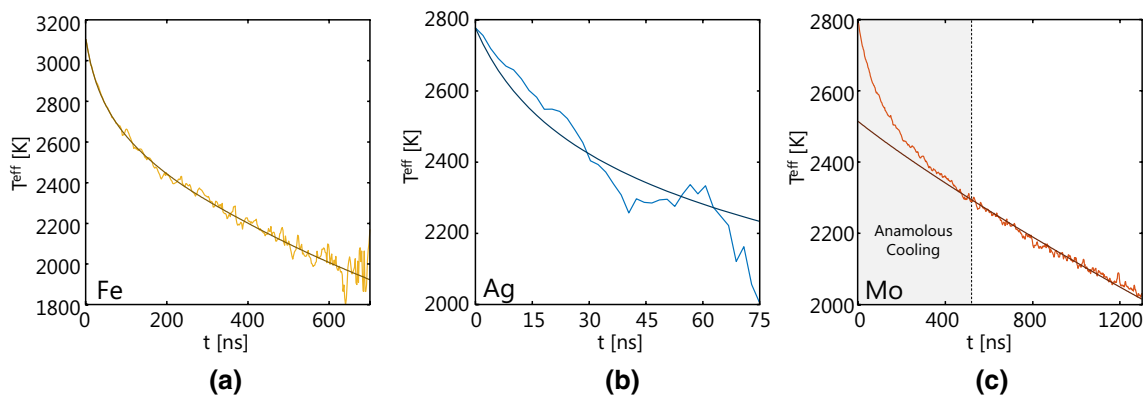
Fig. 10 Temperature decays for **a** Fe–Ar, **b** Ag–Ar, and **c** Mo–Ar. Traces represent an average over 250 shots

nanoparticle sizes are consistent for all three motive gases, as one would expect since the nanoparticle synthesis process is independent of the gas type in this experiment. The sizes obtained using $E(\mathbf{m})_r = 1.1$ are also consistent with values found through ex situ analysis, while sizes obtained using the other $E(\mathbf{m})_r$ values are much smaller. Likewise, the recovered thermal accommodation coefficients, using $E(\mathbf{m})_r = 1.1$, are similar to those reported through previous experimental [12, 14] and molecular dynamics [28] studies. They also follow the expected trends with molecular mass and structural complexity [72, 79], while values found using $E(\mathbf{m})_r = 1.70$ and 1.84 are much smaller. This finding is consistent with results presented in Sect. 4.1, and previous experimental studies that assumed $E(\mathbf{m})_r = 1$ [12, 14]. Figure 10a shows that the simulated temperature decay corresponding to $\mathbf{x}_{MLE}$ for iron nanoparticles in argon is in excellent agreement with the observed pyrometric temperatures calculated assuming $E(\mathbf{m})_r = 1.1$.

The inferred sizes of the silver nanoparticles aerosolized in argon, carbon dioxide, and nitrogen (Table 5) are consistent with one another, ex situ DLS analysis (80 nm), and electron microscopy analysis (65 nm) in the context of the large uncertainties induced by the measurement noise and

model uncertainties. Figure 10b shows that the modelled temperature decay for silver nanoparticles in argon, and the corresponding pyrometrically-defined temperature decay, is much more abrupt compared to that of the iron nanoparticles due, presumably, to a greater degree of evaporative cooling. This observation is consistent with the results of Fillipov et al. [23].

Inspection of the pyrometric temperature decay for molybdenum nanoparticles, e.g., Fig. 10c, reveals a super-exponential decay in the effective temperature that lasts for approximately 400 ns after the laser pulse and cannot be captured by the free molecular heat transfer model proposed in Sect. 2. Superficially, the initial temperature decay curve suggests evaporation-dominated cooling, e.g., Fig. 10a, b for iron and silver nanoparticles in argon, respectively. However, the peak nanoparticle temperatures and the fluence curve in Fig. 7c do not support this hypothesis, since one would expect to see a "plateau region" if evaporative cooling were important in the fluence ranges used in this study. The initial non-exponential temperature decay also resembles "anomalous cooling" effect which is particularly prominent in TiRe-LII measurements carried out at ambient temperatures, e.g., [72], although it typically

Table 5 Maximum likelihood estimates of the nanoparticle size, $d_{p,o}$, in nanometers for silver nanoparticles in various gases

Gas	MLE	Experimental ±	Parameter ±
Ar	76	3	23
N_2	98	6	26
CO_2	78	6	21

Estimates of uncertainty are broken into those resulting from noise in the measured signal and those resulting from model input parameter uncertainty, θ_i. Uncertainties correspond to 95% confidence level (two standard deviations)
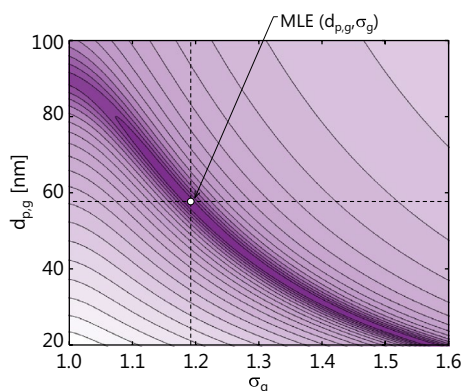
Fig. 11 Log contours of the log-likelihood function considering variation in σ_g and $d_{p,g}$ for Mo–Ar. The contours exhibit similar nonlinear behavior to that observed for silicon nanoparticles by Sipkens et al. [26]

has a shorter duration, ~50 ns. Consequently, this initial temperature decay remains unexplained, and data analysis focuses on effective temperatures starting from 400 ns after the laser pulse.

As noted above, the TAC and the nanoparticle size distribution parameters cannot be inferred simultaneously from TiRe-LII measurements made on molybdenum nanoparticles. Instead, we either infer: (1) the nanoparticle size,

assuming prior knowledge of α; or (2) α, assuming prior knowledge of the nanoparticle size. We first consider the scenario in which the thermal accommodation coefficient is set equal to the MD-derived value of $\alpha = 0.15$ for Mo–Ar reported in Daun et al. [28]. (MD-derived TACs for Mo–N_2 and Mo–CO_2 are unavailable, so nanoparticle sizing is restricted to the Mo–Ar case.) The size distribution found through ex situ analysis (Fig. 5c) suggests a lognormal distribution. The corresponding log-likelihood contours are plotted in Fig. 11 and show a maximum likelihood estimate at $d_{p,g} = 43$ nm and $\sigma_g = 1.34$, consistent with $d_{p,g} = 45$ nm and $\sigma_g = 1.49$ found by electron microscopy. The contours resemble those observed in Sipkens et al. [26] for silicon nanoparticles. Corresponding confidence intervals due to experimental and model parameter uncertainty are summarized in Table 6.

We next consider the opposite scenario, in which the lognormal size distribution found through electron microscopy ($d_{p,g} = 45$ nm, $\sigma_g = 1.49$) is treated as prior knowledge, and used to infer the thermal accommodation coefficient. Table 6 shows the thermal accommodation coefficients for molybdenum nanoparticles in helium, neon, argon, carbon dioxide, and nitrogen. Measurements for molybdenum nanoparticles in monatomic (He, Ne, Ar) and polyatomic (N_2, CO_2) gases were carried out on two non-consecutive days, and Mo–Ar aerosols were measured on both occasions to assess the repeatability of this procedure. The thermal accommodation coefficients for Mo–Ar ($\alpha = 0.24$) are larger than the MD-derived value from Daun et al. [28] ($\alpha = 0.15$).

A comparative analysis of the thermal accommodation coefficients recovered for aerosols of iron and molybdenum nanoparticles in argon, nitrogen, and carbon dioxide also provides useful information about the gas-surface scattering physics that underlie this parameter. Figure 12 shows that the values for Fe–N_2 and Fe–CO_2 are lower than Fe–Ar in the first data set, as expected, since surface energy is accommodated into the internal modes of the polyatomic

Table 6 Maximum likelihood estimates of parameters of interest, x_i, for molybdenum in various gases

θ_i	Gas	x_i	MLE	Experimental ±	Parameter ±	Correlation
$\alpha = 0.15$	Ar	$d_{p,g}$	58	4	44	−0.98
		σ_g	1.19	0.01	0.23	
$d_{p,o} = 45.0\ \sigma_g = 1.49$	He	α	0.05	<0.005	0.01	–
	Ne	α	0.16	<0.005	0.04	–
	Ar	α	0.24	<0.005	0.05	–
	N_2	α	0.18	<0.005	0.06	–
	CO_2	α	0.23	<0.005	0.07	–

Estimates of uncertainty are broken into those resulting from noise in the measured signal and those resulting from sensitivity to input parameters, θ_i. Uncertainties correspond to 95% confidence level (two standard deviations). Diameters are given in nanometers. Reported values are the result of two sets of experiments, with overlapping argon results

Fig. 12 Trends in the MD and experimentally-derived TACs with μ for **a** iron and **b** molybdenum. The TACs from the current study are plotted with MD results from Daun et al. [28] and experimental results from Eremin et al. [12], Kock et al. [14], and Sipkens et al. [16], using values of $E(\mathbf{m}_\lambda)$ taken from Krishnan et al. [39]. Error bounds correspond to model input parameter uncertainty
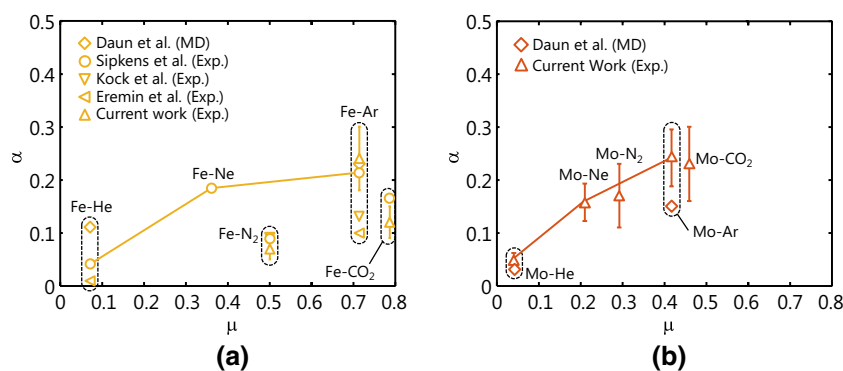
gas molecules less efficiently compared to the translational modes [16, 72, 79]. Figure 12 also shows the present results are consistent with those obtained from reanalyzing data from Ref [16] using $E(\mathbf{m})_r = 1.1$ after truncating the first 30 ns of data and applying Thompson Tau outlier removal, as is done here. The trends are also consistent with TACs reported by Eremin et al. [12] and Kock et al. [14]. Figure 12 also clearly shows that the experimentally-derived TACs for molybdenum nanoparticles in helium, neon, and argon increase monotonically with the ratio between gas molecular mass and surface atomic mass, $\mu = m_g/m_s$, consistent with predictions from molecular dynamics [28] and simple cube models. The TACs between molybdenum nanoparticles and polyatomic gases (N_2, CO_2) are also lower than the trend line for monatomic gases, although the difference is less pronounced compared to the iron aerosols.

5 Conclusions

While time-resolved laser-induced incandescence is mainly used to characterize soot primary particles in combustion applications, it shows promise as a tool for measuring aerosolized metal nanoparticles. Interpreting TiRe-LII data requires reliable spectroscopic and heat transfer models for these types of aerosols, however, which must first be developed. To this end, this study presents a comparative analysis of TiRe-LII measurements on iron, silver, and molybdenum nanoparticles within monatomic and polyatomic gases. These aerosols are produced by pneumatically atomizing nanoparticle colloids, allowing the synthesis of a wide range of aerosols; moreover, decoupling the nanoparticle synthesis from the bath gas facilitates a comparative analysis and provides more insight compared to measurement carried out on nanoparticles synthesized within the gas phase.

The three types of metal nanoparticles chosen for this study have very different thermophysical properties, which are reflected in the variation of peak temperature with fluence. Peak temperatures for molybdenum nanoparticles

increase nearly linearly with increasing fluence, indicating that the absorbed laser energy is transformed into sensible energy of the nanoparticle, while the peak temperature of silver nanoparticles "plateaus" slightly above the boiling point of bulk silver due to evaporative cooling. The peak temperature for iron nanoparticles transitions between these two regimes and plateaus slightly above the boiling point of bulk iron, but this result can be obtained only by assuming that the ratio of $E(\mathbf{m})$ values at the two detection wavelengths close to unity. Otherwise, using radiative properties for bulk molten iron derived from ellipsometry measurements reported in the literature provides non-physical temperatures.

The observed temperature decays for these materials are also characteristic of their respective melting points: The observed temperature decay for molybdenum nanoparticles is consistent with conduction-dominated cooling, while that of the silver nanoparticles is due entirely to evaporation. The temperature decay for iron nanoparticles is due to both evaporative and conductive heat transfer. The active heat transfer modes during cooling also determine the information that can be inferred from TiRe-LII data, as indicated by log-likelihood contour plots. Robust estimates for d_p and α can be obtained from measurements on iron nanoparticles, while only d_p can be found from LII measurements on silver nanoparticles, and independent values of α and d_p cannot be isolated from TiRe-LII measurements on molybdenum nanoparticles. When the TiRe-LII data for molybdenum nanoparticles are analyzed using lognormal size distribution parameters found from ex situ analysis, the resulting TACs follow the expected trends with gas molecular mass and structure, as is the case with the TACs inferred from TiRe-LII measurements on iron nanoparticles. Likewise, the nanoparticle sizes recovered from iron and silver nanoparticles are consistent with those found from ex situ analysis, but, in the former case, again only by assuming an $E(\mathbf{m})_r$ ratio close to unity.

The results of this study support the assertion that TiRe-LII can potentially be developed into a reliable diagnostic for measuring the size and concentration of aerosolized

metal nanoparticles. While it has obvious applications for nanoparticle synthesis and industrial hygiene, TiRe-LII can also be thought of as a scientific instrument for carrying out experiments of fundamental interest, including gas-surface scattering and laser-nanoparticle interactions. Nevertheless, there are several key unresolved questions that require further analysis: Why do the radiative properties of molten iron nanoparticles deviate from those of bulk molten iron? What is responsible for the enhanced absorption cross section of the molten metal nanoparticles? What is the origin of the "anomalous cooling" observed for molybdenum nanoparticles? Answering these questions will require further experimental and theoretical analysis, which will be facilitated through advanced optical diagnostics (e.g., streak cameras, which provide spectrally- and temporally-resolved emissions from the nanoparticles) and numerical simulation tools like Direct Simulation Monte Carlo (DSMC), which can be used to model the complex interaction between evaporated atoms from the nanoparticle and the surrounding bath gas.

References

1. D.L. Feldheim Jr., C.A. Foss, *Metal Nanoparticles: Synthesis, Characterization, and Applications* (Macrel Dekker Inc., Basel, 2002)
2. K.-S. Lee, M.A. El-Sayed, J. Phys. Chem. B **110**, 39 (2006)
3. M. Rai, A. Yadav, A. Gade, Biotechnol. Adv. **27**, 1 (2009)
4. R. Narayanan, M.A. El-Sayed, J. Phys. Chem. B **109**, 26 (2005)
5. W.-X. Zhang, J. Nanopart. Res. **5**, 3–4 (2003)
6. M.T. Swihart, Curr. Opin. Colloid Interface Sci. **8**, 1 (2003)
7. A.D. Maynard, D.Y.H. Pui, *Nanoparticles and Occupational Health* (Springer, Dordreicht, 2007)
8. Y. Ju-Nam, J.R. Lead, Sci. Total Environ. **400**, 1 (2008)
9. J.D. McNeilly, M.R. Heal, I.J. Beverland, A. Howe, M.D. Gibson, L.R. Hibbs, W. MacNee, K. Donaldson, YTAAP **196**, 1 (2004)
10. H.A. Michelsen, C. Schulz, G.J. Smallwood, S. Will, Prog. Energy Combust. Sci. **51**, 2–48 (2015)
11. R.L. Vander Wal, T.M. Ticich, J.R. West, Appl. Opt. **38**, 27 (1999)
12. A. Eremin, E. Gurentsov, C. Schulz, J. Phys. D Appl. Phys. **41**, 5 (2008)
13. A. Eremin, E. Gurentsov, E. Popova, K. Priemchenko, Appl. Phys. B **104**, 2 (2011)
14. B.F. Kock, C. Kayan, J. Knipping, H.R. Orthner, P. Roth, Proc. Combust. Inst. **30**, 1 (2005)
15. A. Eremin, E. Gurentsov, E. Mikheyeva, K. Priemchenko, Appl. Phys. B **112**, 3 (2013)
16. T.A. Sipkens, N.R. Singh, K.J. Daun, N. Bizmark, M. Ioannidis, Appl. Phys. B **119**, 4 (2015)
17. L. Landström, K. Elihn, M. Boman, C.G. Granqvist, P. Heszler, Appl. Phys. A **81**, 4 (2005)
18. J. Knipping, H. Wiggers, B.F. Kock, T. Hülser, B. Rellinghaus, P. Roth, Nanotechnology **15**, 11 (2004)
19. Y. Murakami, T. Sugatani, Y. Nosaka, J. Phys. Chem. A **109**, 40 (2005)
20. T. Sipkens, K.J. Daun, G. Joshi, Y. Murakami, J. Heat Trans. **135**(5), 052401 (2013)
21. A.V. Eremin, E.V. Grentsov, Appl. Phys. A **119**, 2 (2015)
22. J. Reimann, H. Oltmann, S. Will, E. Bassano, L. Carotenuto, S. Lösch, B. H. Günther, Proceeding of the World Congress on Particle Technology, vol 6, Nuremberg, Germany (2010)
23. A.V. Fillipov, M.W. Markus, P. Roth, J. Aerosol Sci. **30**, 1 (1999)
24. N.R. Singh, T.A. Sipkens, K.J. Daun, First Thermal and Fluids Engineering Summer Conference, ASTFE, New York, NY (2015)
25. L. Landström, P. Heszler, J. Phys. Chem. B **108**, 20 (2004)
26. T.A. Sipkens, R. Mansmann, K.J. Daun, N. Petermann, J.T. Titantah, M. Karttunen, H. Wiggers, T. Dreier, C. Schulz, Appl. Phys. B **116**, 3 (2014)
27. K.M. Shvarev, B.A. Baun, P.V. Gel'd, Sov. Phys. Solid State **16**, 11 (1975)
28. K.J. Daun, T.A. Sipkens, J.T. Titantah, M. Karttunen, Appl. Phys. B **112**, 3 (2013)
29. M. Quinten, *Optical Properties of Nanoparticle Systems: Mie and Beyond* (Wiley-VCH, Weinheim, 2011)
30. T.E. Faber, *Introduction to the Theory of Liquid Metals* (Cambridge University Press, Cambridge, 1972)
31. C.F. Bohren, D.R. Huffman, *Absorption and Scattering of Light by Small Particles* (Wiley, New York, 1983)
32. T.C. Bond, R.W. Bergstrom, Aerosol Sci. Technol. **40**, 1 (2006)
33. F. Migliorini, K.A. Thomson, G.J. Smallwood, Appl. Phys. B **104**, 2 (2011)
34. H.A. Michelsen, F. Liu, B.F. Kock, H. Bladh, A. Boiarciuc, M. Charwath, T. Dreier, R. Hadef, M. Hofmann, J. Reimann, S. Will, P.-E. Bengtsson, H. Bockhorn, F. Foucher, K.-P. Geigle, C. Mounaim-Rousselle, C. Schulz, R. Stirn, Tribalet Appl. Phys. B. **87**, 3 (2007)
35. J.C. Miller, Philos. Mag. **20**, 168 (1969)
36. S. Krishnan, G.P. Hansen, R.H. Hauge, J.L. Margrave, High Temp. Sci. **29**, 1 (1990)
37. H. Kobatake, H. Khosroabadi, H. Fukuyama, Met. Trans. A **43**, 7 (2012)
38. K.J. Daun, Met. Trans. A. **47**, 7 (2016)
39. S. Krishnan, K.J. Yugawa, P.C. Nordine, Phys. Rev. B **55**, 13 (1997)
40. K.M. Shvarev, V.S. Gushchin, B.A. Baum, High Temp. **16**(1–3), 441–446 (1978)
41. P.F. Paradis, T. Ishikawa, Y. Nosaka, Int. J. Thermophys. **23**, 2 (2002)
42. M.F. Modest, *Radiative Heat Transfer*, 3rd edn. (Academic Press, New York, 2003)
43. B.T. Barnes, JOSA **56**, 11 (1966)
44. D.W. Juenker, L.J. LeBlanc, C.R. Martin, J. Opt. Soc. Am. **58**, 2 (1968)
45. E.D. Palik, *Handbook of Optical Constants of Solids* (Elsevier, London, 2012)
46. R.S. Hixson, M.A. Winkler, M.L. Hodgdon, Phys. Rev. B **42**, 10 (1990)
47. A.V. Grosse, A.D. Kirshenbaum, J. Inorg. Nucl. Chem. **24**, 6 (1962)
48. P.D. Desai, J. Phys. Chem. Ref. Data **15**, 3 (1986)
49. C. Cagran, W. Wilthan, G. Pottlacher, Thermochim. Acta **445**, 2 (2006)

50. J.A. Dean, *Lange's Handbook of Chemistry*, 15th edn. (McGraw-Hill, New York., 1999)
51. F. Mafune, J.-Y. Kohno, Y. Takeda, T. Kondow, J. Phys. Chem. B **107**, 18 (2003)
52. W.M. Haynes (ed.), *CRC Handbook of Chemistry and Physics, 96th Edition, 2015–2016* (CRC Press, Cleveland, 2015)
53. P.D. Desai, J. Phys. Chem. Ref. Data **16**, 1 (1987)
54. D.A. Young, B.J. Alder, Phys. Rev. A **3**, 1 (1971)
55. B.J. Keene, Int. Mater. Rev. **33**, 1 (1988)
56. R. Novakovic, E. Ricci, D. Giuranno, A. Passerone, Surf. Sci. **576**, 1 (2005)
57. H.M. Lu, Q. Jiang, J. Phys. Chem. B **109**, 32 (2005)
58. S. Velasco, F.L. Román, J.A. White, A. Mulero, FFE **244**, 1 (2006)
59. TSI, Model 3076 Constant Output Atomizer Instruction Manual (2005)
60. Y. Liu, S.A. Majetich, R.D. Tilton, D.S. Scholl, G.V. Lowry, Environ. Sci. Technol. **39**, 5 (2005)
61. F. He, D. Zhao, Environ. Sci. Technol. **41**, 17 (2007)
62. P.C. Lee, D. Meisel, J. Phys. Chem. **86**, 17 (1982)
63. S.K. Friedlander, C.S. Wang, J. Colloid Interface Sci. **22**, 2 (1966)
64. W.K. Brown, K.H. Wohletz, J. Appl. Phys. **78**, 4 (1995)
65. A.D. Rakić, A.B. Djurišić, J.M. Elazar, M.L. Majewski, Appl. Opt. **37**, 22 (1998)
66. M.A. Ordal, R.J. Bell, R.W. Alexander, L.L. Long, M.R. Querry, Appl. Opt. **24**, 24 (1985)
67. T. Phenrat, H.J. Kim, F. Fagerlund, T. Illangasekare, R.D. Tilton, G.V. Lowry, Environ. Sci. Technol. **43**, 15 (2009)
68. R. Thompson, J. R. Stat. Soc. **47**, 1 (1985)
69. S.W. Churchill, R. Usagi, AIChE J. **18**, 6 (1972)
70. S. Maffi, S. De Iuliis, F. Cignoli, G. Zizak, Appl. Phys. B **104**, 2 (2011)
71. D.R. Snelling, K.A. Thomson, F. Liu, G.J. Smallwood, Appl. Phys. B **96**, 4 (2009)
72. K.J. Daun, G.J. Smallwood, F. Liu, J. Heat Trans. **130**(12), 121201 (2008)
73. G. Schierning, R. Theissmann, H. Wiggers, D. Sudfeld, A. Ebbers, D. Franke, V.T. Witusiewicz, M. Apel, J. Appl. Phys. **103**, 8 (2008)
74. P.R. Couchman, W.A. Jesser, Nature **269**, 481–483 (1977)
75. D.R. Snelling, F. Liu, G.J. Smallwood, Ö.L. Gülder, Combust. Flame **136**, 1 (2004)
76. J.P. Perdew, Phys. Rev. B **37**, 11 (1988)
77. P.J. Hadwin, T.A. Sipkens, K.A. Thomson, F. Liu, K.J. Daun, Appl. Phys. B **122**, 1 (2016)
78. B.M. Crosland, M.R. Johnson, K.A. Thomson, Appl. Phys. B **102**, 1 (2011)
79. K.J. Daun, Int. J. Heat Mass Transf. **52**, 21 (2009)